# Decoupling the Kinetic Essence of Iron-Based Anodes through Anionic Modulation for Rational Potassium-Ion Battery Design

*Meng Ma, Kai Yao, Yikun Wang, Dina Fattakhova-Rohlfing, Shaokun Chong**

M. Ma, Y. Wang, Prof. S. Chong
Frontiers Science Center for Flexible Electronics, Institute of Flexible Electronics, Northwestern Polytechnical University, Xi'an 710072, China
E-mail: iamskchong@nwpu.edu.cn (Prof. S. Chong)

K. Yao, Prof. D. Fattakhova-Rohlfing
Forschungszentrum Jülich GmbH, Institute of Energy and Climate Research, Materials Synthesis and Processing IEK-1, 52425 Jülich, Germany

Keywords: potassium-ion batteries, anode materials, iron compounds, ionic diffusion, solid electrolyte interphase

Abstract: Potassium-ion batteries (PIBs) have favorable characteristics in terms of cell voltage and cost efficiency, making them a promising technology for grid-scale energy storage. The rational design of suitable electrode materials on a theoretical basis, aiming at high power and energy density, is of paramount importance to bring this battery technology to the practical market. In this paper, a series of iron-based compounds with different non-metal anions are selectively synthesized to investigate the nature of kinetic differences induced by anionic modulation. A combination of experimental characterization and theoretical calculation reveals that iron phosphide, with its moderate adsorption energy ($E_a$) and lowest diffusion barrier ($E_b$), exhibits the best cycling and rate properties at low electrochemical polarization, which is related to the narrow $\Delta d$-$p$ band center gap that facilitates ion transfer. In addition, the optimization of the electrolyte formula results in the carbon-supported iron phosphide anode running stably over 2000 cycles at 0.5 A $g^{-1}$ and exhibiting a high rate capacity of 81.1 mAh $g^{-1}$ at 2 A $g^{-1}$. The superior electrochemical properties are attributed to the robust KF-rich solid electrolyte interphase formed by the highly compatible KFSI-EC/DEC configuration.

## 1. Introduction

The rapid growth of the electrical vehicle market and the increasing demand for grid-scale facilities have driven the search for a secondary battery technology with high energy density and low cost. Potassium-ion batteries (PIBs) as an alternative to next-generation lithium-ion batteries (LIBs) have real potential for large-scale electrical energy storage due to the high potassium content in the earth's crust (~2.1 wt%), significant cost efficiency and attractive redox potential ($E^0_{K/K^+}$ = -2.936 V *vs.* standard hydrogen electrode (SHE)).[1-3] Negative electrodes (anodes) play a crucial role in the performance of PIBs, and great efforts have been invested in the research and development of appropriate materials. Carbonaceous materials based on an intercalation mechanism were pioneered for study as PIB anodes, but their limited capacity is not sufficient to meet the growing energy demand.[4,5] Other anode materials with higher theoretical capacity based on conversion and alloying mechanisms have therefore received more attention. However, these materials investigated so far exhibit unsatisfactory cycling stability, especially at high rates, due to severe volume expansion and mechanical degradation during repeated insertion and extraction of potassium ions.[6-8] For this reason, spatial confinement of conversion/alloying active anode materials in conductive carbon substrates has emerged as the most widely investigated tactic to effectively optimize cycling stability. However, the improved cyclability is achieved at the expense of capacity, as the extensive use of lightweight carbon materials reduces the volumetric energy density of the whole electrode.[9,10] Therefore, the search for more efficient anode active materials based on theoretical screening and rational design is of great importance for improving the prospects of PIBs.

General, the transport of potassium ions in the anode side during the electrochemical reaction can be divided into two main steps: adsorption and diffusion. More specifically, the $K^+$ ions first migrate through the electrolyte in an applied electric field, adsorb on the anode surface by physical or chemical interaction, and then diffuse into the interior of the active material to be reduced, which involves two key parameters: the $K^+$ adsorption energy ($E_a$) and the diffusion energy barrier ($E_b$).[11,12] In this course, if the anode materials have a weak tendency to adsorb potassium ions, even with a high conductivity, there will not to be enough alkali ions for the subsequent redox reaction, which means low electrochemical activity and inferior charge storage capacity.[13] Conversely, a terrible diffusion ability always leads to the massive accumulation of adsorbed potassium ions on the anode surface but hardly transfer to the interior, which causes two serious issues: sluggish dynamic behavior with severe polarization leading to unqualified rate capability; and excessive parasitic side reactions with electrolyte components

causing low initial Coulombic efficiency (ICE), rapid capacity attenuation, and even electronically isolation of the active material. In short, there may be some equilibrium constraints between these two factors during battery operation. Considerations on this "adsorption-diffusion" balance and the essence of its role in electrode functionality has piqued our research interest and led to a series of experimental explorations.

Apart from the nature of electrode material itself, the transport of $K^+$ ions is also influenced by the interfacial solid electrolyte interphase (SEI), as the solvated ions must pass through the SEI layer where they are desolvated to react with the anode active material, a process that is particularly aided by the inorganic crystal components of the SEI.[14] More importantly, the SEI composition is highly dependent on the electrolyte, such that adjusting the electrolyte formulation, including the organic solvent, functional additive, and salt type and concentration, can alter the SEI layer in terms of ion transport, mechanics, and passivation behavior, leading to significant differences in the performance of a given electrode. Taking the graphene anode as an example, it is believed that the common ether-based electrolyte, owning a higher lowest unoccupied molecular orbital (LUMO) energy level, can readily induce a stable inorganic-dominated SEI compared to the ester counterpart.[15,16] However, the strong co-intercalation of solvated K-ions ($[K\text{-solvent}]^+$) in ethers will result in decreased capacity and increased operating voltage of the graphene anode.[17] Furthermore, the susceptibility of ether-based solvents to oxidation at high potentials restricts their use in full cells with practical high-voltage cathode active materials.[18] Therefore, it is worth investigating how electrolyte configurations can be customized for specific electrode materials based on existing ester solvents.

Bearing the abovementioned points in mind, herein, we selected a series of iron (Fe)-based conversion anodes (FeP, $FeS_2$, and $Fe_2O_3$) with varied non-metal anions as case studies, which feature comparable capacities and moderate volumetric variation compared to insertion- and alloying-type anode active materials, and systematically investigated the ion transport behavior of these compounds during potassium storage and delved into the essence behind their differences, which in turn provides a selection criterion for anode candidates. Combined density functional theory (DFT+U) calculation with electrochemical performance test, it is confirmed that the appropriate $E_a$ and $E_b$ play a crucial role in improving the rate performance. The moderate adsorption and strong diffusivity can ensure the efficient transport of K-ion from the surface to the bulk of FeP with guaranteed capacity and redox kinetics. Therefore, FeP exhibits a promising capacity of 188.9 mAh $g^{-1}$ at 0.02 A $g^{-1}$ and still retains 51.7% of the initial capacity when the current density increases to 0.2 A $g^{-1}$, with a much weaker polarization compared to $FeS_2$ and $Fe_2O_3$. Further theoretical calculations on the iron 2d and anion 2p band centers

uncovers that such a diversity in diffusion ability largely stems from the disparate Δ*d-p* energy gaps, and a lower energy gap in FeP favors electronic exchange to promote the redox kinetics. Furthermore, the in-depth XPS reveals that KFSI-EC/DEC is a more compatible electrolyte configuration for the FeP@NC anode surviving over 2000 cycles due to the rational salt-derived SEI composition. The charge storage mechanism of a typical conversion reaction ending with the potassiation products of $K_3P$ and Fe is revealed by an ex-situ study.

## 2. Results and Discussion

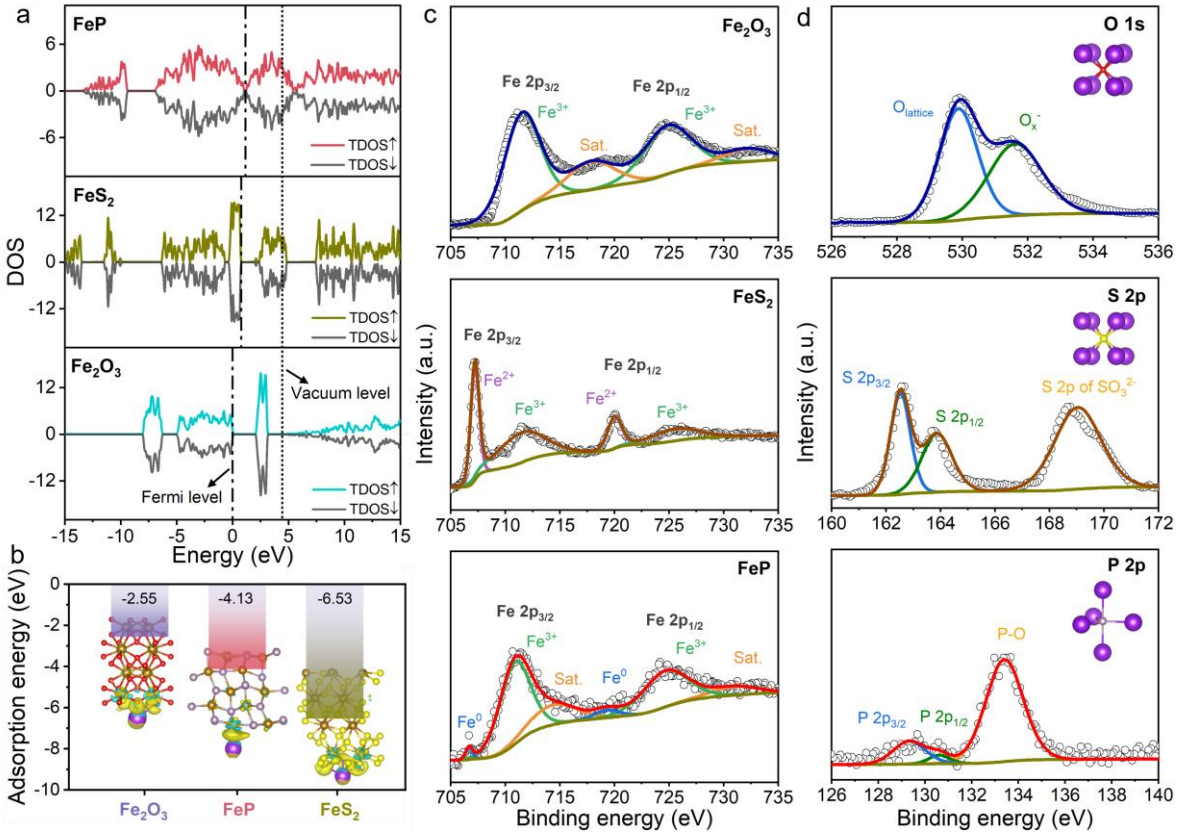


**Figure 1.** Theoretical computation and structure characterization. a) DOS of FeP, $FeS_2$, and $Fe_2O_3$; b) adsorption energies of $K^+$ on FeP (110), $FeS_2$ (111), and $Fe_2O_3$ (110) surfaces with corresponding charge difference illustrations; XPS spectra of c) cation (Fe 2p) and d) anion (O 1s, S 2p, P 2p) deconvolution for FeP, $FeS_2$ and $Fe_2O_3$. Here, brown, gray, yellow, red, and purple balls represent iron, phosphide, sulfur, oxide, and potassium atoms, respectively.

Methodological prediction of potential electrode candidates in terms of the electronic structure is a pivotal tool to guide and simplify practical experiments. Herein, density functional theory augmented by the Hubbard U (DFT+U) method was consulted to predict the application potentials of three iron-based compounds, FeP, $FeS_2$, and $Fe_2O_3$, as conversion anodes for PIBs. Firstly, the density of states (DOS) for three materials was computed, and the resulting data is

presented in **Figure 1**a and Figure S1, Supporting Information. The energy band structure are in a normalized arrangement according to the vacuum level. Notably, both FeP and $Fe_2O_3$ exhibit antiferromagnetic configurations, while $FeS_2$ adopts a low-spin configuration, consequently yielding zero net magnetic moments for all three compounds. The bandgap width directly reflects the material's electrical conductivity, constituting a key metric in the evaluation of electrode materials, given that high conductivity usually corresponds to weak polarization behavior. It is clearly that FeP boasts a Fermi level that traverses the density of states, thereby classifying it as a conductor. In contrast, the bandgap widths for $Fe_2O_3$ and $FeS_2$ are determined to be 2.2 and 1.0 eV, demonstrating the semiconductor property. Moreover, the Fermi level's precise elevation is directly entwined with the open-circuit voltage of batteries. Closer proximity to the vacuum energy level means higher open-circuit voltage in a full battery configuration, which is critical for anode electrodes as it contributes to higher energy density when matched with cathodes. FeP features the Fermi level closest to the vacuum level, rendering it the most promising, followed by $FeS_2$, and lastly, $Fe_2O_3$. Furthermore, the electrochemical activity of electrode materials typically correlates with its propensity for adsorbing alkaline ions. As shown in Figure 1b, an examination was conducted regarding the adsorption energies ($E_a$) of potassium-ion on the lowest-energy crystal surfaces (110) of $Fe_2O_3$, (110) of FeP, and (111) of $FeS_2$, yielding values of -2.6, -4.1, and -6.5 eV, respectively, showing spontaneous adsorption processes. Corresponding adsorption structures and charge differences are also graphically illustrated in the inset of Figure 1b. Nevertheless, the values of FeP and $FeS_2$ are more negative than that of $Fe_2O_3$, indicating the stronger potassium affinity and the capability to adsorb more potassium atoms, which thermodynamically provides a higher probability for the occurrence of subsequent redox reaction. Therefore, from a theoretical point of view, it is found that the $K^+$ transfer behaviors on various iron compounds are quite different, may leading to distinct electrochemical properties, and the correlation between them needs to be further verified by practical experiments.

Experimentally, three kinds of iron-based compounds were fabricated via an analogical two-step method. Typically, ferrous sulfate ($FeSO_4$) was dispersed in a mixed glycerol-water solution to form a quasi-emulsion system, in which Fe (II)-glycerol aggregates acted as nucleation and growth centers, guiding the subsequent generation of hierarchical α-FeOOH precursors.[19] The as-prepared α-FeOOH was then subjected to high-temperature heating treatments to obtain distinct iron-based compounds. Specifically, FeP and $FeS_2$ were synthesized through the associated gaseous phosphorization and sulfuration processes, while $Fe_2O_3$ was obtained by calcining FeOOH under an air atmosphere. The detailed crystalline

information of synthesized samples were characterized by X-ray diffraction (XRD), as provided in **Figure 2**a. The recorded diffraction patterns accord well with the orthorhombic FeP (PDF#65-2595), cubic $FeS_2$ (PDF#42-1340), and hexagonal $Fe_2O_3$ (PDF#33-0664), respectively.[6,20,21] The corresponding Raman spectra show the positions of characteristic phonon lines in good accordance with the reported data, further evidencing the successful production of pure iron-based compounds (Figure S2, Supporting Information).[22-24] Furthermore, the chemical composition and electronic states on the surface of these samples were analyzed by X-ray photoelectron spectroscopy (XPS). In Figure 1c, the distinct peak locations of deconvoluted Fe 2p orbitals reflect different valance states of Fe. In the case of FeP, the main peaks located at 711.0 and 724.8 eV can be readily identified to $Fe^{3+}$ $2p_{3/2}$ and $Fe^{3+}$ $2p_{1/2}$, whereas the small peaks at 706.8 and 719.4 eV are associated with the formation of $Fe^0$ during pyrolysis.[25] The Fe in $Fe_2O_3$ is also present in trivalent form. For $FeS_2$, $Fe^{2+}$ that coordinated with $S_2^{2-}$ dimers accounts for a significantly greater ratio, while the existence of small amounts of $Fe^{3+}$ originates from the slight air oxidation.[26] Meanwhile, the corresponding high-resolution P 2p, S 2p, O 1s XPS spectra are illustrated in Figure 1d, of which P 2p peaks can be deconvoluted into two bands at 129.3 eV and 130.7 eV for P $2p_{3/2}$ and P $2p_{1/2}$, and S 2p can be annotated by two signals of $2p_{3/2}$ (162.7 eV) and $2p_{1/2}$ (163.9 eV), as well as the O 1s curve shows bands at 529.9 and 531.6 eV that associated with the lattice oxygen atom ($O_{lattice}$) and the adsorbed oxygen ($O_x^-$).[26-28] The composition of valence bonds plays a fundamental role in determining the number of potassium ions involved in the redox reaction, thereby ruling on the potassium storage capacity. During the electrode working, cations mainly bond with electrons, while anions devote to coordinate with potassium ions. The $Fe^{3+}$/Fe redox pairs expect to conjunct more electrons than $Fe^{2+}$/Fe. The anion-potassium coordination structures are shown in the inset of Figure 1d, it can be seen that one oxygen, sulfur, and phosphorus atoms are coordinated to four, four, and five potassium atoms, corresponding to the mol volumes of 101.9, 64.8, and 139.7 $Å^3$, respectively. Considering the relative atom mass of S > P > O, the mass specific capacity of iron oxide should be the highest, while iron sulfide may prevail in volume specific capacity (Figure S3, Supporting Information).

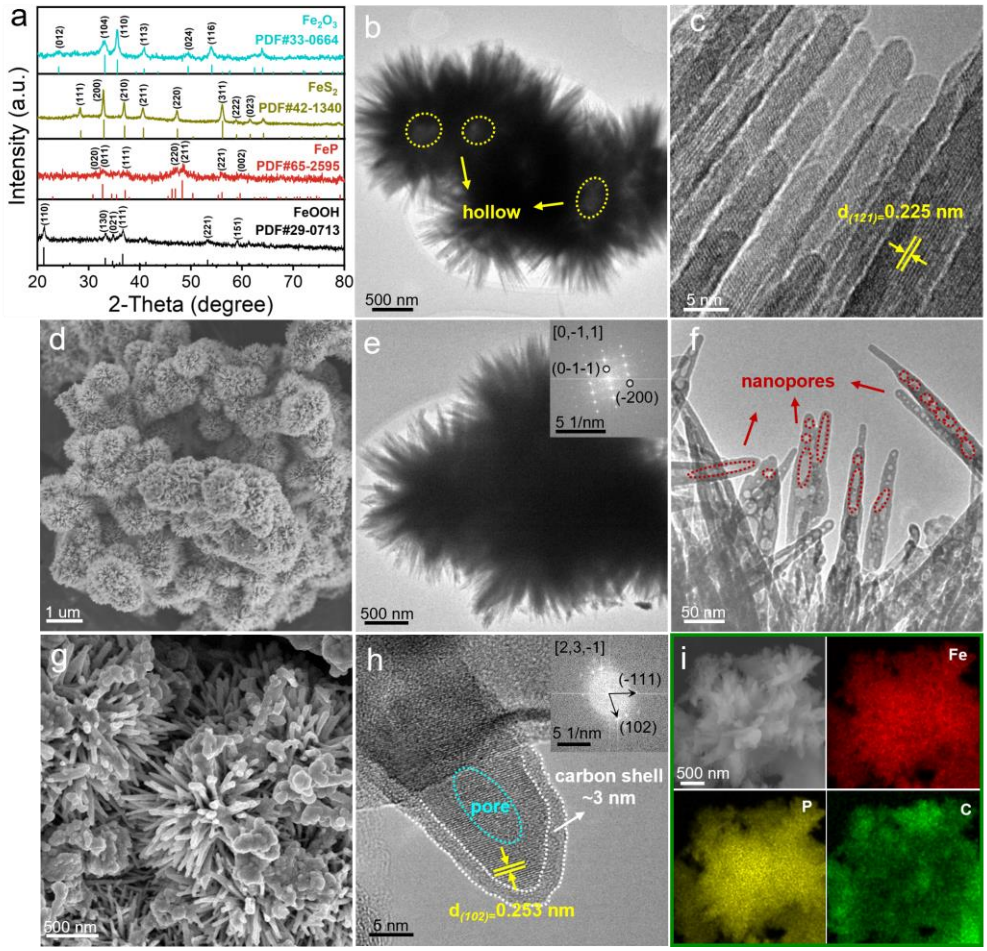


**Figure 2.** Crystallography and morphology characterization. a) XRD patterns of the prepared FeOOH, FeP, $FeS_2$, and $Fe_2O_3$; b-c) TEM images for FeOOH; d) SEM and e-f) TEM images with FFT inset for FeP; g) SEM, h) HRTEM with FFT inset, and i) EDS mapping for carbon assisted FeP.

The morphologies and nanometric structures of as-fabricated samples are characterized via scanning electron microscopy (SEM) and transmission electron microscopy (TEM). The α-FeOOH precursor exhibits a hierarchical micro spherical flower architecture assembled by nanosheets in Figure 2b-c and Figure S4, Supporting Information. The high-resolution TEM (HRTEM) image highlights the characteristic that these nanosheets are formed by a number of nanorods, where lattice fringes with a d-spacing of 0.225 nm agree with the (121) facet of FeOOH. After phosphating, the hierarchical structure remains almost unchanged in Figure 2d-f, except for the appearance of numerous nanopores in the surrounded rods, which is believed to offer convenient diffusion paths for ionic transport.[22] The other two iron-based rivals exhibit similar morphological characteristics to FeP as displayed in Figure S5, Supporting Information. It is well known that cooperating with carbonenous matrix is a critical approach to optimize the performance of electrodes, considering its positive role in spatial confinement and conductivity

improvement. Therefore, coating FeP with a thin nitrogen-doped carbon (NC) layer decomposed from dopamine hydrochloride was synthesized to construct a FeP@NC composite for subsequent electrolyte engineering study. FeP@NC preserves the flower-like morphology assembled by nano-rods, while the slight agglomeration on the surface may be attributed to the inhomogeneous deposition of carbon in Figure 2g-i. HRTEM images reveal that the internal FeP nanorods with well-defined lattice fringes are enveloped in the external carbon layer with a thickness of around 3 nm. The d-spacing of 0.253 nm in combination with fast Fourier transform (FFT) spots demonstrates that the clear fringes belong to the (102) facet of orthorhombic FeP. What's more, the energy-dispersive X-ray spectroscopy (EDS) elemental mapping images confirm the homogenous distribution of Fe, P, and C elements in the composite, suggesting the presence of carbon coating on FeP particles, as expectation.

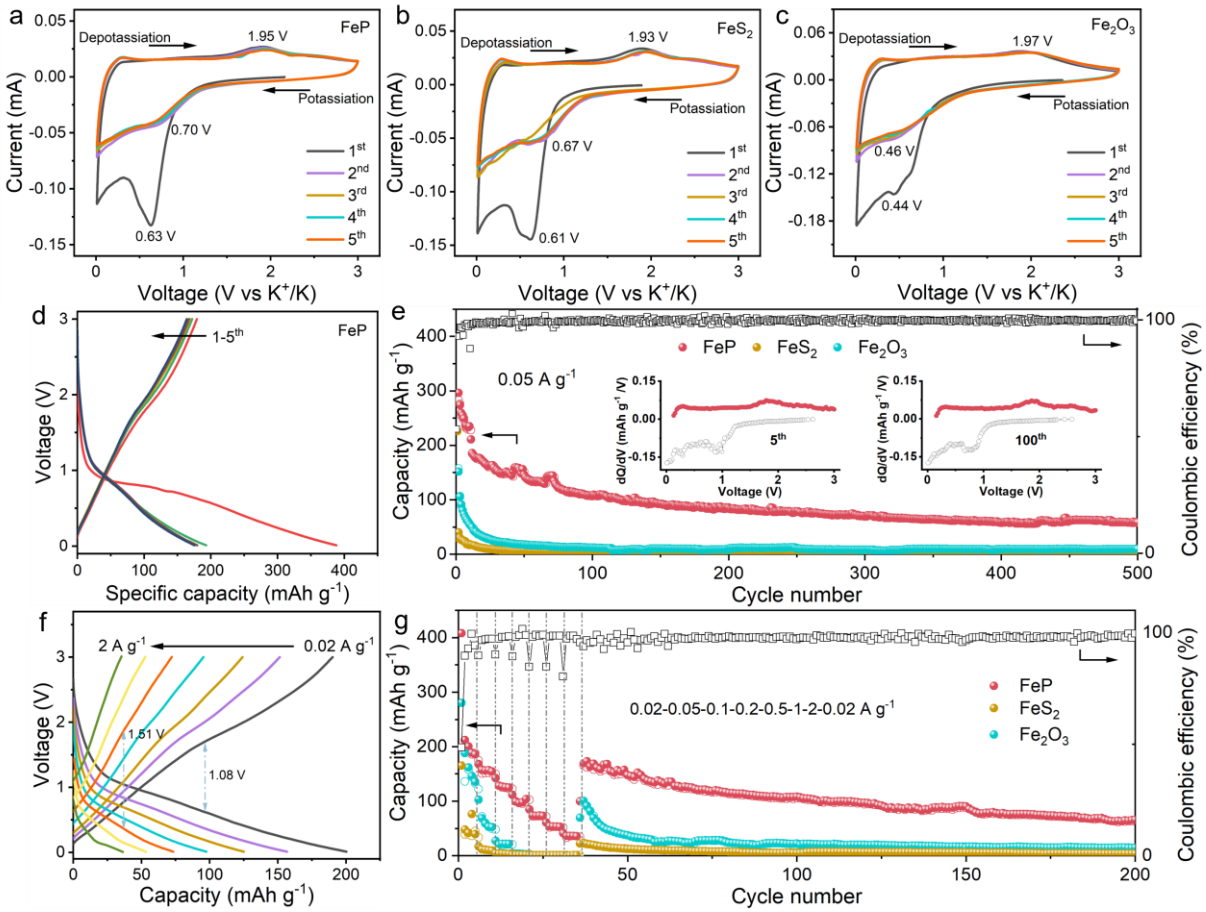


**Figure 3**. Electrochemical performances. CV curves of a) FeP, b) $FeS_2$, and c) $Fe_2O_3$; d) charge-discharge profiles of first five cycles for FeP at 0.05 A $g^{-1}$; e) cycling performances at 0.05 A $g^{-1}$; f) charge-discharge profiles of FeP at various current densities; g) rate performances.

The electrochemical characteristics of iron-based compounds were evaluated against K metal anode with the electrolyte of 1.0 M KFSI in ethylene carbonate (EC)/ diethyl carbonate (DEC) (1/1 by volume) in PIB coin half cells. Cyclic voltammogram (CV) curves of FeP, $FeS_2$ and

$Fe_2O_3$ at a scan rate of 0.1 mV $s^{-1}$ within the voltage window of 0.01-3.0 V are shown in **Figure 3**a-c. The initial cathodic peaks of three samples vary considerably with the subsequent scans, which is associated with the irreversible side reaction and the formation of solid electrolyte interphase (SEI) film during the first potassiation process. The broad cathodic peaks at around 0.7, 0.67 and 0.46 V correspond to the conversion reactions of FeP, $FeS_2$ and $Fe_2O_3$, respectively. In the reverse anodic scans, the peak at about 1.9 V represents the deconversion reactions from K-based products to metallic K and Fe-based compounds. Moreover, more severe voltage hysteresis are observed in $FeS_2$ and $Fe_2O_3$ samples compared to FeP, which is assigned to their sluggish redox kinetics. Additionally, the highly overlapped charge-discharge profiles after initial cycle confirms the superior reversibility of FeP (Figure 3d and Figure S6, Supporting Information). The cycling stability of three anodes under a current density of 0.05 A $g^{-1}$ are displayed in Figure 3e. The pure FeP electrode delivers a high discharge capacity of 283.6 mAh $g^{-1}$ and great cyclic stability over 500 cycles with an average Coulombic efficiency of 99.3%, corresponding to a low capacity decline rate of 0.159% per cycle. Comparatively, $FeS_2$ and $Fe_2O_3$ counterparts undergo rapid capacity decay, falling to single digit after 100 cycles. The illustrations show the basically identical dQ/dV curves of the $5^{th}$ and the $100^{th}$ cycles for FeP, further confirming the electrode stability in the course of cycling. Besides, the level of voltage hysteresis of FeP varies less as per the current density compared to other two electrodes, around 0.43 V from 0.02 to 0.5 A $g^{-1}$, indicating a lower polarization between the charge and discharge processes, which is due to the efficient redox kinetics and reversibility (Figure 3f). The detailed capacities at various rates are demonstrated in Figure 3g, in which the FeP yields 188.9, 156.7, 125.2, 97.7, 73.4, 53.3, 36.4 mAh $g^{-1}$ at current densities of 0.02, 0.05, 0.1, 0.2, 0.5, 1.0, 2.0 A $g^{-1}$, respectively, significantly superior to $FeS_2$ and $Fe_2O_3$. Correspondingly, a high capacity retention of 51.7% can be realized for FeP anode at 0.2 A $g^{-1}$ relative to the initial capacity at 0.02 A $g^{-1}$, while those for $FeS_2$ and $Fe_2O_3$ are almost zero. When the current density falls to 0.02 A $g^{-1}$ again, the FeP anode can recover a high reversible capacity of 172.9 mAh $g^{-1}$, approaching the original level, and still have a capacity residue of 65.5 mAh $g^{-1}$ over 200 cycles, suggesting the outstanding electrode structural integrity at high current pulse.

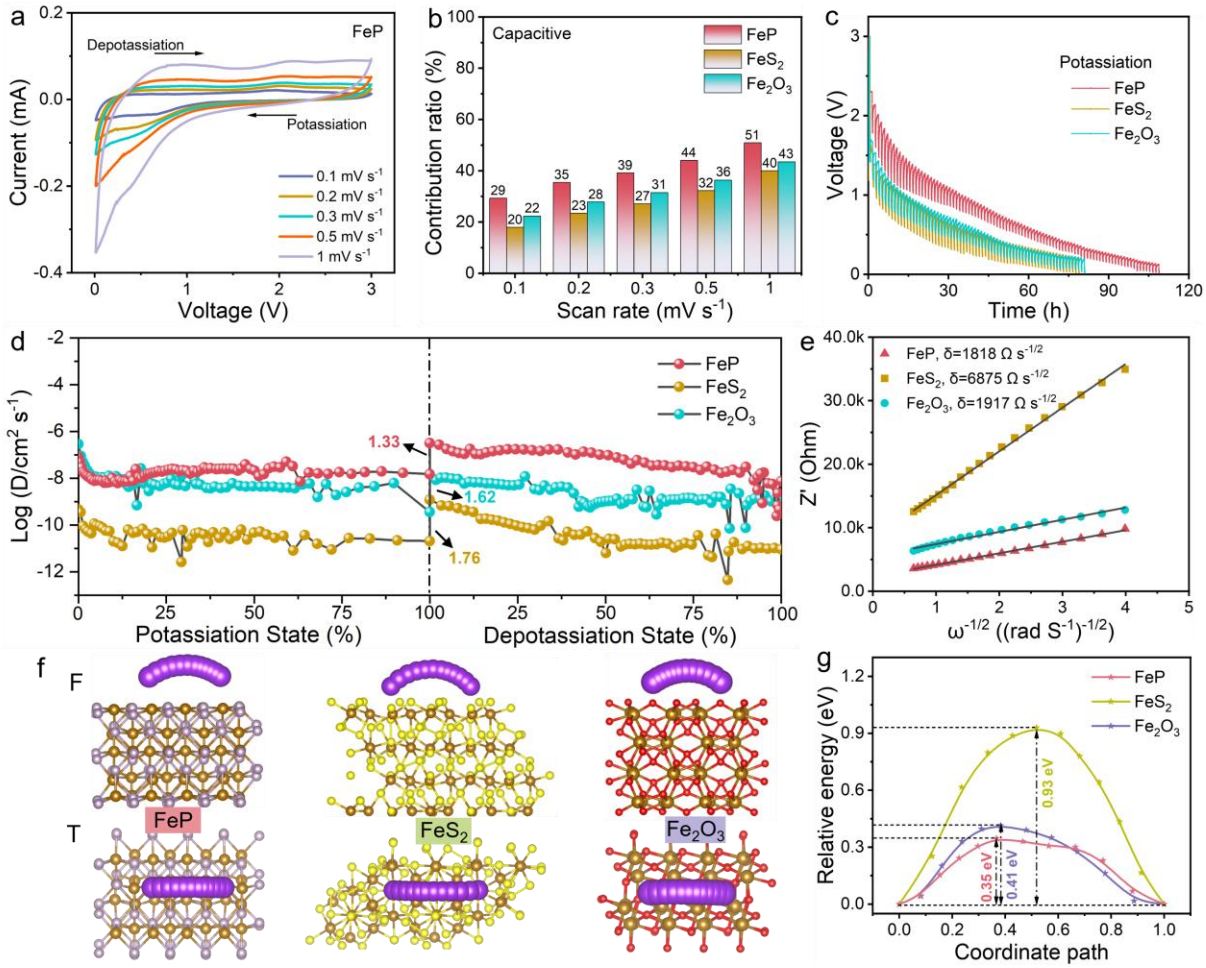


**Figure 4.** Electrochemical kinetics. a) CV curves of FeP electrode at different scan rates; b) contribution ratio of the capacitive-controlled capacity of FeP, $FeS_2$, and $Fe_2O_3$ at different scan rates; c) GITT profiles for potassiation and d) the calculated diffusion coefficient of three samples during potassiation and depotassiation processes; e) $Z'$ as a function of $\omega^{-1/2}$ in the semi-infinite region for calculation of Warburg coefficient (σ); f) front and top view schematic representations of K-ion diffusion pathways for three samples, where brown, gray, yellow, red, and purple balls represent iron, phosphide, sulfur, oxide, and potassium atoms, respectively; and g) the corresponding energy distribution diagram.

Further investigation and comparison to $K^+$ migration kinetics are necessary to gain insights into the potassium storage difference. CV measurements of three electrodes at various scans were evaluated first, as shown in **Figure 4**a and Figure S7, Supporting Information. It can be seen that the potential differences and intensities of all redox peaks gradually increase with the scan rates from 0.1 to 1 mV $s^{-1}$, owning to the augmented polarization inside the electrodes. And the integral area of curve corresponds to the total amount of $K^+$ storage that usually contributed by two parts of capacity: the diffusion-controlled redox reaction capacity and the surface-controlled pseudo-capacitance. The linear relationship of peak current ($i_p$) and the

square root of the scan rates ($v^{1/2}$) indicating the apparent $K^+$ diffusion coefficient ($D_{K^+}$) can be calculated by Randles-Sevcik equation:[29]

$$i_p = 2.69 \times 10^5 n^{3/2} A C_0 D^{1/2} v^{1/2} \quad (1)$$

in which $i_p$ is the peak current density, $n$ is the electron-transfer number per molecule formula during the redox reaction, $A$ is the surface area of the electrode, $C_0$ is the concentration of $K^+$ in the electrode, and $v$ is the scan rate. As shown in Figure S8, Supporting Information, the FeP anode displays the larger slope ($i/v^{1/2}$) than $FeS_2$ and $Fe_2O_3$ during potassium process, suggesting a faster $K^+$ diffusion kinetics. In addition, the log($i$)-log($v$) for three samples show a good linear relationship, where the calculated $b$ values are basically closer to 0.5, qualitatively identifying the diffusion-dominant electrochemical behavior, which is normal for the non-carbon assisted electrodes (Figure S9, Supporting Information). Compared to $K_1$ referring to "capacitive behavior", the larger value of $K_2$ referring to "diffusion behavior", especially at a redox potential of 0.8 V, also validates this point (Figure S10, Supporting Information). Furthermore, the quantitative contribution ratios of capacitive capacities for three samples at various scan rates are provided in Figure 4b, presenting a trend of progressive increase. The FeP shows higher capacitive fractions under random scan rates compared to others, which is favorable to the rapid surface potassium-storage behavior. Analogously, galvanostatic intermittent titration technique (GITT) measurement further confirms the dynamics advantage of iron phosphide (Figure 4c). The single titration schematic at 1.05 V labeled with related parameters and the calculated values of overall process are displayed in Figure 4d and Figure S11, Supporting Information. In comparison with $FeS_2$ and $Fe_2O_3$, FeP exhibits a greater $K^+$ migration coefficient ($D_{K^+}$) of $10^{-8}$~$10^{-7}$ $cm^2$ $s^{-1}$ in the course of potassiation and depotassiation. Additionally, electrochemical impedance spectroscopy (EIS) technology was also employed to analyze the ionic transfer capability after working (Figure S12, Supporting Information). Each Nyquist plot consists of a semicircle at high- and middle-frequency regions as well as a sloping tail at the low-frequency region that represent the charge-transfer and mass-transfer processes of potassium ions, respectively. The charge-transfer resistance ($R_{ct}$) of FeP obtained by fitting with the electrical equivalent circuit is around 192.3 Ω, significantly smaller than the values of other anodes. It is also worth mentioning that the calculated Warburg coefficient ($\delta w$) in the low-frequency semi-infinite region shows a smaller value for the FeP electrode (Figure 4e). All of the above electrochemical dynamic analyzation indicates that potassium ions diffuse more efficiently in iron phosphide than in oxide and sulfide.

To better figure out the dynamic difference essence of various compounds, the computational simulations of the diffusion barriers ($E_b$) of working ions on three iron compounds were carried

out using a transition state (TS) search. The front and top view images of ionic migration on the FeP (110), $FeS_2$ (111) and $Fe_2O_3$ (110) crystal facets are illustrated in Figure 4f. The diffusion of K-ion on all of these materials follows a basic arcuate curve from one stable point to another, with the maximum point located in the middle of the path. From the energy distribution profiles in Figure 4g, it can be seen that the ease degree of potassium ions diffusion follows FeP > $Fe_2O_3$ > $FeS_2$. The maximum energy barrier of 0.93 eV for $FeS_2$ exactly accounts for the experimental observations showing the lowest $D_{K^+}$ value. On the contrary, the lowest energy barrier of FeP (merely 0.35 eV) manifests the fastest $K^+$ diffusion and conversion reaction dynamics. Combined with the foregoing adsorption energy of $FeS_2$ > FeP > $Fe_2O_3$, we found that the balanced relationship of $E_a$ and $E_b$ is vital in enhancing the charge-storage kinetics, and the FeP with the moderate K affinity and strongest diffusion capability ensures the most efficient ionic transport from electrolyte to electrode inside, resulting in the best electrochemical performances. Moreover, the nature of the superior diffusivity of FeP is further revealed by analyzing the density of electronics states in the iron 2d and anions 2p bands, as shown in Figure S13, Supporting Information. A minimum energy gap ($\Delta p$-$d$ = 1.19 eV) between the p-band center and d-band center can be observed in FeP anode, implying the minimized energy required for bond breaking, which is conductive to the electronic exchange, and thus promoting fast charge-storage redox kinetics.[11, 30]

A compatible electrolyte configuration is essential for anode materials to achieve qualified performances, considering its function on generating competent SEI layers with good ionic conductivity and electronic insulation, while acting as a passivation membrane to protect the internal active electrode from successive reaction and depletion with electrolyte. FeP@NC was synthesized as the research target, and its electrochemical performances were investigated in two kinds of electrolytes, KFSI-EC/DEC and $KPF_6$-EC/DEC. The initial five CV curves obtained at 0.1 mV $s^{-1}$ are displayed in **Figure 5**a and Figure S14, Supporting Information. Clearly distinct irreversible regions can be observed for two electrolytes upon the first potassiation process, with a more visible cathodic peak (~0.62 V) in KFSI instead of $KPF_6$-based electrolyte, indicting different SEI layers. After first cycle, reversible cathodic peaks (~0.64 V) and anodic peaks (~1.96 V) both exist in two electrolytes, which are attributed to the conversion and de-conversion reactions of FeP as mentioned. From the galvanostatic discharge-charge profiles (Figure 5b and Figure S15, Supporting Information), the initial CE (ICE) of FeP@NC anode in KFSI-EC/DEC electrolyte can be calculated to 53.2%, significantly higher than that of 38.3% in the $KPF_6$ counterpart. The low ICE may result from the formation of thick SEI film. Additionally, the curves after first cycle overlap better in KFSI-based electrolyte,

suggesting a higher electrode reversibility. Furthermore, the effect of salts on electrochemical performances were evaluated via cycle and rate tests with various current densities from 0.02 to 2 A $g^{-1}$. Cycled at 0.5 A $g^{-1}$, the batteries in KFSI- and $KPF_6$-based electrolytes deliver the $10^{th}$ discharge capacities of 192.4 and 96.8 mAh $g^{-1}$, and remain residual capacities of 142.1 and 13.9 mAh $g^{-1}$ after 400 cycles, corresponding to the capacity retentions of 73.9% and 14.6%, respectively (Figure 5c). Through a structural reorganization-induced attenuation stage in Figure S16, Supporting Information, the KFSI electrolyte-filled battery eventually outputs an ultra-long lifespan over 2000 cycles with stable capacity of ~90 mAh $g^{-1}$, demonstrating the outstanding cyclability. Whereas the battery fitted with $KFP_6$ salt suffers from a continuous loss of capacity, which may be due to the ineffective passivation of the formed SEI film causing the overreaction and constant consumption of electrolyte. Besides, the battery cycled in $KPF_6$ exhibits inferior rate performance with severe polarization phenomenon (Figure S17, Supporting Information). By comparison, the battery cycled in KFSI shows small polarization voltages with the increase of current densities, from 0.86 V at 0.02 A $g^{-1}$ to 1.30 V at 0.5 A $g^{-1}$, as well as superior rate capability of 291.9, 243.7, 222.9, 190.3, 148.6, 115.0 and 81.1 mAh $g^{-1}$ at 0.02, 0.05, 0.1, 0.2, 0.5, 1 and 2 A $g^{-1}$, respectively (Figure 5d-e). Even back to 0.02 A $g^{-1}$, it still delivers the capacity of 286.7 mAh $g^{-1}$ that comparable to the value at initial 0.02 A $g^{-1}$, indicating the high stability of anode in KFSI-based electrolyte. It is also interesting to note that due to the incidental temperature change in test, we obtained the capacity data of the battery at different temperatures. The KFSI battery undergoes a capacity decline from 287.7 to 218.2 mAh $g^{-1}$ as the temperature drops from 25 $^{o}$C to 0 $^{o}$C. When the temperature goes back up, it recovers to around 255 mAh $g^{-1}$ and keeps stable to 410 cycles (Figure S18, Supporting Information). CV tests at various scans and GITT measurements further confirm the advantages of KFSI-EC/DEC electrolyte on electrochemical dynamics (Figure 5f-g and Figure S19, Supporting Information). Such a stark contrast of potassium-storage behavior can be attributed to the difference of SEI generated in the surface of anodes.

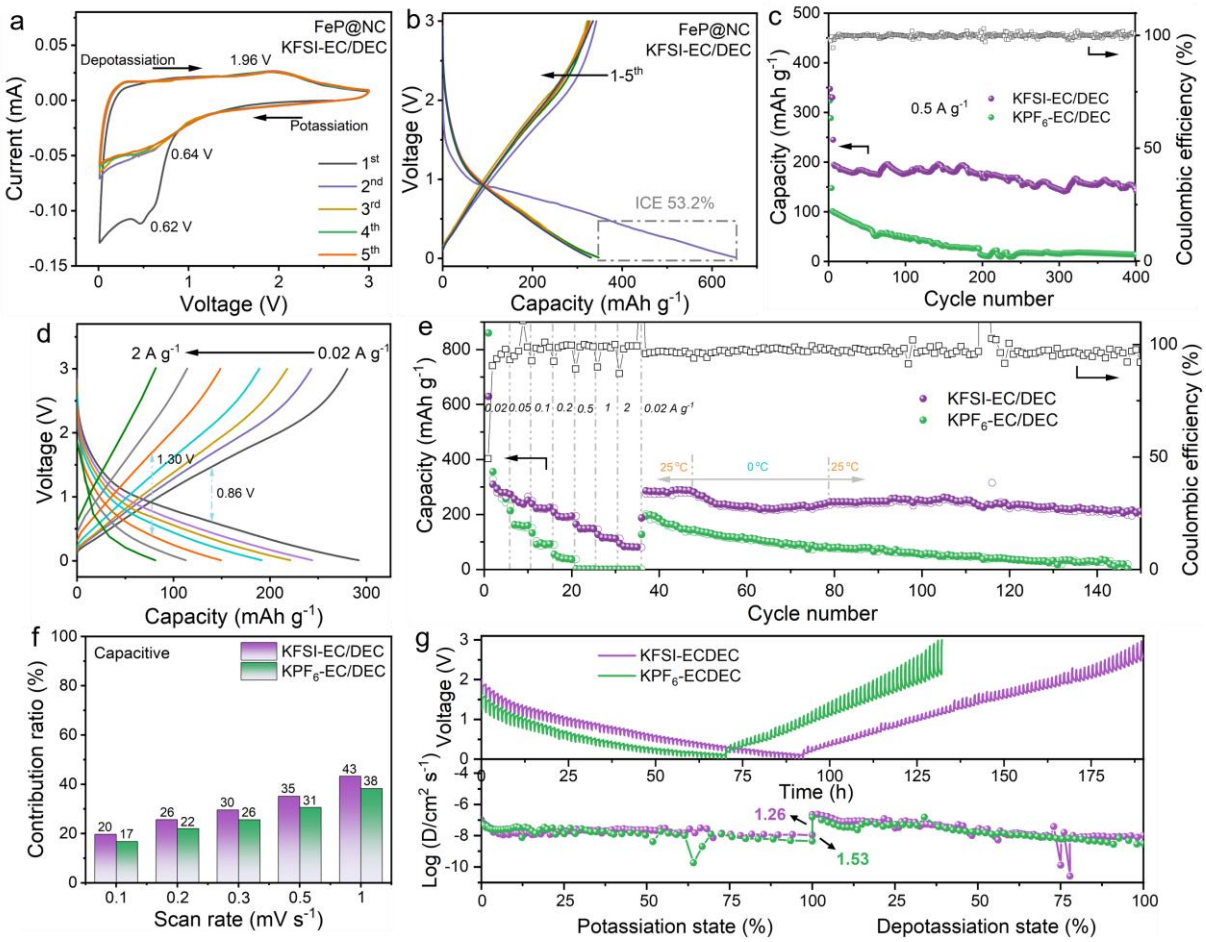


**Figure 5.** Electrochemical performances of FeP@NC anode at different types of electrolytes. a) CV curves; b) charge-discharge profiles of first five cycles for FeP@NC at KFSI-based electrolyte at 0.02 A $g^{-1}$; c) cycling performances at 0.5 A $g^{-1}$ after precycling 3 loops at 0.02 A $g^{-1}$; d) charge-discharge profiles at various current densities; e) rate performance; f) contribution ratio of the capacitive-controlled capacity at different scan rates; g) GITT curves and calculated diffusion coefficient during potassiation and depotassiation processes.

It is well-known that $KPF_6$ is hardly hydrolyzed, so the SEI layer formed by $KPF_6$-based electrolytes basically originates from solvent-induced reduction.[31] In addition, the LUMO energy level of KFSI is lower than those of EC and DEC, indicative of the more readily reactive feature of KFSI salt during SEI formation.[32] In order to further understand the correlation between electrolyte type and electrochemical properties, in-depth XPS was conducted to analyze the chemical composition of the SEI layers derived by various electrolyte salts. It can be seen from C 1s spectra (**Figure 6**a and 6d) that there are five deconvolution peaks at 284.8, 286.6, 287.8, 289.1, and 290.1 eV, corresponding to C-C, ROK, C-O-C, C=O, and RO-COOK bonds, which are sourced from potassium oligomers, potassium alkyl carbonates and alkoxides decomposed by solvent and salt.[33,34] It should be noted that the C 1s signals of SEI components overlap with those of binder and conductive carbon additive, but the integrated intensity for the

carbon species in KFSI was still significantly lower than that in $KPF_6$. Especially after sputtering, the carbon species in KFSI are nearly negligible except for the C-C bond in graphite, while those in $KPF_6$ remain almost unchanged. It can therefore be inferred that the surface carbon-containing layer derived from KFSI-based electrolyte is thinner, which is exactly responsible for its higher ICE. O 1s spectra in Figure 6b and 6e also show C=O, C-O, and ROOK bonds from salt and solvent decomposition.[34] Note that the ROOK content in KFSI shows a downshift tendency from 23.05% to 3.83% during sputtering, while for $KPF_6$ it drops from 26.32% to 18.00%, indicating that less organic components are generated in the KFSI-derived SEI and gradually decrease with increasing sputtering depth. The $KPF_6$-derived SEI with thick organic layer features poor ionic conductivity and cannot efficiently passivate the anode electrode, ultimately leading to unsatisfactory electrode properties. On top of that, two characteristic peaks corresponding to K-F and S-F/P-F are detected in the F 1s spectra of two electrolytes in Figure 6c and 6f, where S-F and P-F originate from the residual $FSI^-$ and $PF_6^-$, and K-F signals refer to potassium fluoride (KF) that holds a positive influence on stabilizing the anode, due to its high chemical stability, low solubility, strong shear modulus, and high electronic insulation.[32] On the pristine surface of SEI film, the intensity of K-F bond in KFSI is clearly higher than that in $KPF_6$, and further intensifies after etching for 10 nm. Combined with O 1s results, it can be concluded that the SEI films induced by two kinds of electrolytes are both typical of a layered distribution structure with organic outside and inorganic inside. However, due to the distinct SEI formation mechanisms in these two electrolytes, various interfacial components are generated, which further leads to the discrepancies in final electrode functionality. In KFSI-EC/DEC, mainly low LUMO energy level KFSI salts are involved in the formation of SEI membranes, thus producing more salt-derived KF. For $KPF_6$-EC/DEC, in contrast, it is mainly free solvent molecules that take part in SEI generation, but highly free organic solvent molecules easily trigger severe side reactions and more organic SEI components, causing low Coulombic efficiency and capacity attenuation.[35,36]

The electrochemical performance of full batteries based on FeP// $K_{0.7}Mn_{0.4}Li_{0.1}Co_{0.125}Ni_{0.125}Fe_{0.125}Cu_{0.125}O_2$ configuration were further tested, as shown in Figure S20, Supporting Information. During the voltage range of 0.5-3.5 V, the full cell shows superior rate capability. At 0.1 A $g^{-1}$, a considerable long-term cycling stability can also be achieved with a good capacity retention of ~70% after 200 cycles, demonstrating a promising application potential. In terms of the charge-storage mechanism of FeP, it has been recognized that there is a certain microstructure and size dependence of the potassium-storage reaction for anode materials, and the detailed potassiation intermediate and final products, $K_xP$, of

phosphides have not yet been unified in related studies.[37-40] Thus, ex-situ TEM and XRD were consulted to elucidate the reaction mechanism and phase transition in the hierarchal FeP anode during the potassiation/depotassiation process in KFSI-EC/DEC electrolyte. The HRTEM images and corresponding selected area electron diffraction (SAED) patterns obtained in fully discharged (0.01 V) and charged (3.0 V) states are presented in Figure 6g-j. At 0.01 V, the SAED image demonstrates the presence of $K_3P$ and Fe as final products, and the plane spacing of the lattice fringes can be further fitted to the (111), (002), and (110) facets of $K_3P$ (JCPDS No. 74-0128) and the (110) facet of Fe, respectively. Conversely, only characteristic diffraction rings and lattice fringes belonging to FeP phase can be detected when recharged to 3.0 V, which is confirmed by XRD tests (Figure S21, Supporting Information). These results indicate that the K-storing procedure of this hierarchal FeP anode follows a typical conversion mechanism with the equation of $FeP + 3K^+ + 3e^- \leftrightarrow K_3P + Fe$, in which Fe is served as redox center permitting 3-eletron transfer per formula.

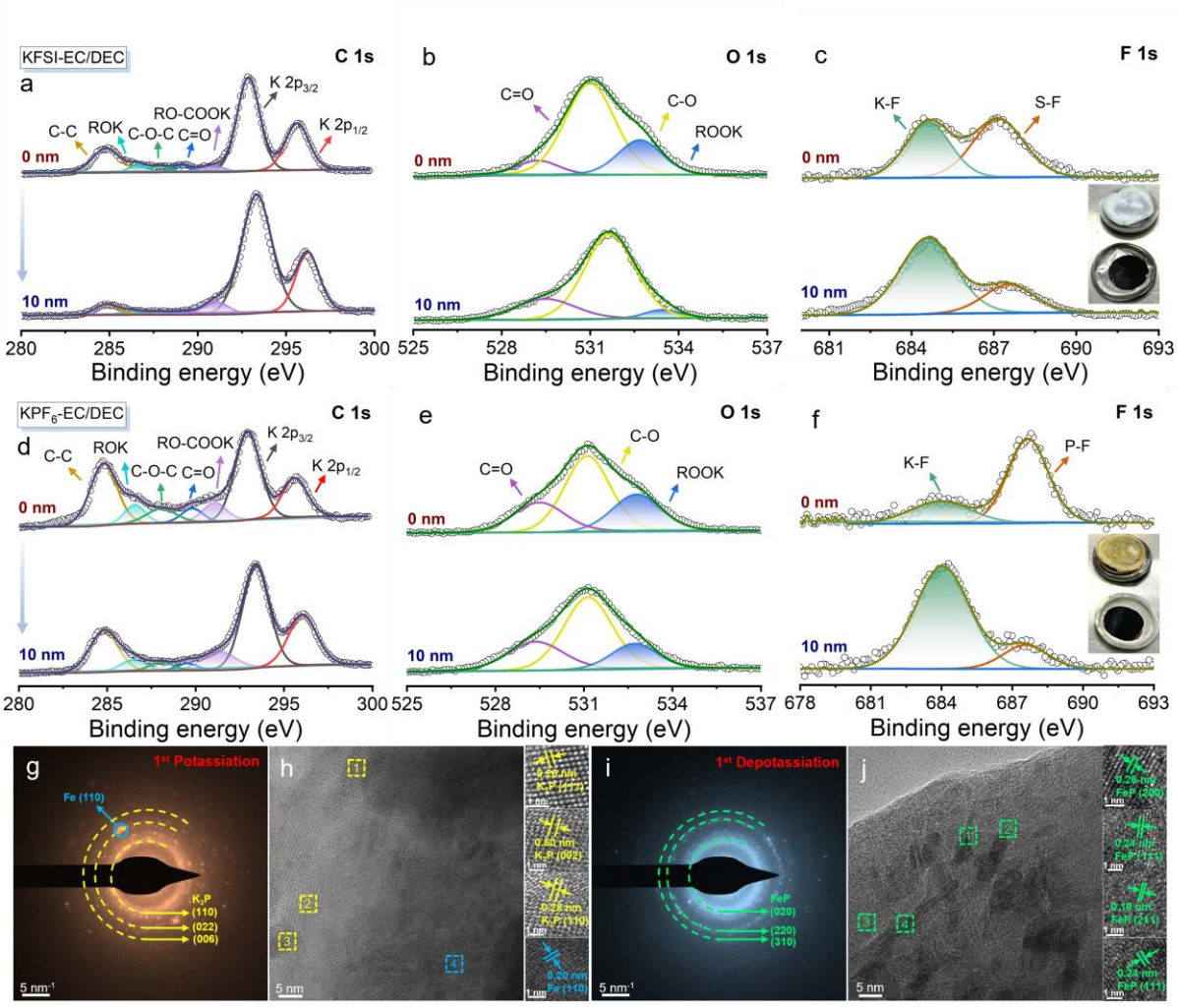


**Figure 6.** Electrochemical mechanism of FeP@NC anode. Depth-profiling XPS spectra of a) C 1s, b) O 1s, and c) F 1s of SEI harvested from KFSI-EC/DEC electrolyte; depth-profiling

XPS spectra of d) C 1s, e) O 1s, and f) F 1s of SEI harvested from $KPF_6$-EC/DEC electrolyte. Insets on the right of each panel are the digital photos of each sample; g) SAED pattern and h) HRTEM images after the initial fully potassiation state; i) SAED pattern and j) HRTEM images after the initial fully depotassiation state.

## 3. Conclusion

In summary, for fundamentally understanding the kinetics deference of potassium-ion transfer process, a series of iron-based compounds (FeP, $FeS_2$, and $Fe_2O_3$) are selectively synthesized, and the intrinsic correlation between anionic variation and the corresponding electrode performance is systematically studied. Combined experiment and theoretical computation confirm that FeP exhibits superior cycling and rate capabilities with weak polarization behavior among these Fe-based compounds, which is benefited from the equilibrium "$E_a$-$E_b$" relationship, i.e., the moderate adsorption energy and lowest diffusion barrier that originated from the narrow $\Delta p$-$d$ band center, favorable for efficient K-ionic transfer kinetics. Additionally, the KFSI-based electrolyte modifying strategy gives rise to the generation of thin and robust solid electrolyte interphase with rational chemical composition, which plays a critical role in protecting the active electrode and boosting the interfacial ionic transport, ultimately endowing the carbon-assisted FeP anode with excellent reversibility over 2000 cycles and high rate capability of 81.1 mAh $g^{-1}$ at 2 A $g^{-1}$. Ex situ test result verifies that K-ion insertion-extraction is proceeded via a conversion mechanism with the potassiation product of $K_3P$ and Fe, in which Fe is responsible for the charge compensation. This study offers a viable criterion for screening and designing the candidate electrodes for high-performance PIBs, and emphasizes the importance of electrolyte engineering in fulfilling electrode functionality, which can also be generalized to the development of other battery systems.

## Experimental Section

### Materials Synthesis:

The preparation of FeP, $FeS_2$, and $Fe_2O_3$: FeOOH precursor was synthesized through a typical hydrothermal method. First of all, $FeSO_4$ (111 mg, Aladdin, 99.9%) was added to a mixed solvent of water (37 mL) and glycerol (3 mL). After stirring for 10 min, the uniform solution was transferred into a Teflon-lined autoclave (50 mL) and maintained at 120 °C for 24 h. Then the hydrothermal precipitate was washed and freeze-dried to collect FeOOH precursor.

Afterward, FeOOH was phosphatized with $NaH_2PO_2$ as a phosphorus source to synthesize the FeP sample. Specifically, the obtained FeOOH and $NaH_2PO_2$ in a mass ratio of 1:5 were putted into two separate porcelain boats with $NaH_2PO_2$ at the upstream side and FeOOH at the downstream side of the furnace, heated at 450 °C under Ar with a ramp rate of 1 °C $min^{-1}$ for 3 h. In a same calcination procedure, the $FeS_2$ sample can be prepared by replacing $NaH_2PO_2$ with S powder. Additionally, the fabrication of another control sample, $Fe_2O_3$, follows the similar synthesis process, except for annealing the FeOOH precursor without any additions in an air atmosphere.

The preparation of FeP@NC: Typically, 121 mg Tris was firstly dissolved into the 100 mL de-ionized water, and 15 μL HCl was added to form a uniform solution by continuously stirring for 1h. After that, 30 mg dopamine hydrochloride and 50mg FeP powder were dispersed in the above solution and stirred for 24 h. The resultant polydopamine-coated FeP product was collected by centrifugation and washed repeatedly with de-ionized water and alcohol. Then, the FeP@NC complex can be collected after calcining at 500 °C under Ar for 3h.

**Material Characterizations:**

X-ray diffraction (XRD) was measured to detect the crystal structure of samples by a Bruker D8 Advance diffractometer equipped with a monochromatized Cu-Kα radiation (λ = 1.5418 Å) in the 2θ ranging from 20° to 80°. Field emission scanning electron microscopy (FESEM) images were acquired with a ZEISS Gemini SEM 300 microscope to analyze the surface microscopic characterizations of samples. High-resolution transmission electron microscopy (HRTEM) images with more microstructure information were recorded by FEI Talos F200X operated at 200 kV. Raman measurements were performed by a Nanofinder 30 microscope with a laser excitation wavelength of 532 nm. X-ray photoelectron spectroscopy (XPS) was conducted on VG MultiLab 2000 instrument to detect the element chemical state on the sample surface. The standard binding energy of C 1s (284.6 eV) was applied for calibration. For in-depth XPS, the electrodes charged to 3 V (vs. $K^+/K$) were sputtered by $Ar^+$ ion beam for 10 nm and then measured the internal elemental states.

**Electrochemical Measurements:**

The electrochemical performances of active materials were measured in CR2025 coin-type cells, which were assembled in an argon-filled glove box, using a metallic potassium foil as the counter electrode, and a Grade GF/D Whatman glass microfiber filter as the separator. The working anode electrodes were prepared by pasting the mixture of active materials, acetylene black and Poly(vinylidene fluoride) at a mass ratio of 7/2/1 onto a Cu foil, vacuum-drying at 80°C, and then punching to 12 mm disks with an average loading of around 1.0 mg $cm^{-2}$. Two

different electrolytes were injected, including 1.0 M KFSI in ethylene carbonate (EC)/ diethyl carbonate (DEC) (1/1 by volume), and 0.8 M $KPF_6$ in EC/DEC (1/1 by volume). The amount of electrolyte for each cell was 120 μL. After setting the assembled coin-type batteries aside for 12 h, galvanostatic charge-discharge and galvanostatic intermittent titration (GITT) measurements were performed with a multichannel Neware battery testing system between 0.01 and 3.0 V versus $K^+/K$. In GITT tests, the cells were discharged/charged with a pulse current of 0.01 A $g^{-1}$ for 10 min, and then relaxed under open circuit for 60 min. This sequence was continued between 0.01 and 3.0 V. Cyclic voltammetry (CV) and electrochemical impedance spectroscopy (EIS) were recorded by CHI660. For the full-cell test, P3-$K_{0.7}Mn_{0.4}Li_{0.1}Co_{0.125}Ni_{0.125}Fe_{0.125}Cu_{0.125}O_2$ was prepared via a sol-gel method as the positive electrode. To prepare the working cathode electodes, active P3-$K_{0.7}Mn_{0.4}Li_{0.1}Co_{0.125}Ni_{0.125}Fe_{0.125}Cu_{0.125}O_2$, acetylene black and Poly(vinylidene fluoride) binder with a mass ratio of 7/2/1 were milled into a homogeneous slurry with an adequate amount of NMP, which was then coated onto an Al foil, vacuum-dried at 80°C and punched to 12 mm disks with an average loading of around 3.0 mg $cm^{-2}$. Before assembling the full cell, the FeP@NC anode was initially cycled at 0.01-3.0 V in a half-cell to remove the irreversible capacity, while the P3-$K_{0.7}Mn_{0.4}Li_{0.1}Co_{0.125}Ni_{0.125}Fe_{0.125}Cu_{0.125}O_2$ cathode was initially cycled at 1.5-4.2 V for activation. The N/P ratio is 1.12/1 to avoid the excessive K plating on anode, corresponding to the mass loading ratio of ~1/3. The full cells were tested between 0.5 and 3.5 V using 1.0 M KFSI-EC/DEC electrolyte.

CV tests at various scans: Capacitive effect was evaluated qualitatively from the following relationship between the scan rate (v) and the measured current (i):

$$i = av^b \quad (1)$$

$$\log i = b\log v + \log a \quad (2)$$

in which *a* and *b* are empirical parameters.

The specific contribution ratio of capacitive behavior can be quantitatively calculated by:

$$i = k_1 + k_2 v^{1/2} \quad (3)$$

in which $k_1$ and $k_2$ are constants, $k_1 v$ and $k_2 v^{1/2}$ stand for the capacitive and diffusion contribution, respectively.

GITT measurements: The apparent diffusion coefficients of K-ion ($D_{K+}$) were measured by Fick's second law:

$$D = 4/\pi\tau \left(\frac{m_B V_M}{M_B A}\right)^2 \left(\frac{\Delta E_S}{\Delta E_\tau}\right)^2 \quad (4)$$

in which, $m_B$, $V_M$, $M_B$, and $A$ mean the mass, molar volume, molecule weight of active material, and the electrochemically active surface area of electrode, respectively. $\tau$ is the current pulse duration. $\Delta E_\tau$ is the deviation voltage arising from the current pulse, and $\Delta E_S$ is the deviation of equilibrium voltage after each current pulse.

EIS measurements: From EIS spectra, Warburg diffusion coefficient ($\sigma$), negatively correlated to the rate of potassium ion diffusion in the material, can be obtained by:

$$\omega = 2\pi f \quad (5)$$

$$Zre = R + \delta\omega^{-1/2} \quad (6)$$

$$D = 0.5R^2T^2/A^2n^2F^4C^2\delta^2 \quad (7)$$

in which $f$ is test frequent, $\omega$ is angular frequent, $R$ is gas constant, and $Zre$ is the real part of the impedance, $D$ is diffusion coefficient of $K^+$, $T$ is Kelvin temperature, $A$ is area of electrodes, $F$ is Faraday constant, $n$ is electronic transfer number per molecule, and $C$ is molar concentration of $K^+$.

**DFT Calculations:**

All simulations were conducted using density functional theory (DFT) implemented in the CASTEP. The Perdew-Burke-Ernzerhof (PBE) exchange-correlation function of the generalized gradient approximation (GGA) was employed for calculations, and ultrasoft pseudopotentials were utilized. An energy cutoff of 500 eV was selected to ensure energy convergence to $1\times10^{-5}$ eV. K-points were determined using the Monkhorst-Pack method. Convergence criteria for energy, force, stress, and displacement were set to $1.0\times10^{-5}$ eV/atom, 0.03 eV/Å, 0.05 GPa, and 0.001 Å, respectively. DFT+U was applied to assess the electronic structure, with U values for Fe 3d set to 5.3, 2, and 4.9 for $Fe_2O_3$, $FeS_2$, and FeP, respectively. The initial electronic configuration for $Fe_2O_3$ and $FeS_2$ was set to antiferromagnetic, while FeP was set to high spin. The transition state (TS) search method was employed for diffusion path calculations. Visualization of atomic structure and electron density difference was performed using VESTA.

**Supporting Information**

Supporting Information is available from the Wiley Online Library or from the author.

**Acknowledgements**

This work was supported by National Natural Science Foundation of China (52207248), China Postdoctoral Science Foundation (2021TQ0266 and 2022M722606), Natural Science Basic

Research Program of Shaanxi (2022JQ-113), Guangdong Basic and Applied Basic Research Foundation (2022A1515010208 and 2021A1515110164).

Received: ((will be filled in by the editorial staff))

Revised: ((will be filled in by the editorial staff))

Published online: ((will be filled in by the editorial staff))

References

[1] T. Hosaka, K. Kubota, A. S. Hameed, S. Komaba, *Chem. Rev.* **2020**, *120*, 6358-6466. https://doi.org/10.1021/acs.chemrev.9b00463.

[2] M. Ma, S. Chong, K. Yao, H. K. Liu, S. X. Dou, W. Huang, *Matter* **2023**, *6*, 3220-3273. https://doi.org/10.1016/j.matt.2023.07.009.

[3] Z. Yang, J. Zhang, M. C. W. Kintner-Meyer, X. Lu, D. Choi, J. P. Lemmon, J. Liu, *Chem. Rev.* **2011**, *111*, 3577-3613. https://doi.org/10.1021/cr100290v.

[4] D. A. Gribble, Z. Li, B. Ozdogru, E. McCulfor, Ö. Ö. Çapraz, V. G. Pol, *Adv. Energy Mater.* **2022**, *12*, 2103439. https://doi.org/10.1002/aenm.202103439.

[5] W. Zhang, M. Sun, J. Yin, K. Lu, U. Schwingenschlögl, X. Qiu, H. N. Alshareef, *Adv. Energy Mater.* **2021,** *11*, 2101928. https://doi.org/10.1002/aenm.202101928.

[6] H. Wu, S. Lu, S. Xu, J. Zhao, Y. Wang, C. Huang, A. Abdelkader, W. A. Wang, K. Xi, Y. Guo, S. Ding, G. Gao, R. V. Kumar, *ACS Nano* **2021,** *15*, 2506-2519. https://doi.org/10.1021/acsnano.0c06667

[7] W. Feng, H. Wang, Y. Jiang, H. Zhang, W. Luo, W. Chen, C. Shen, C. Wang, J. Wu, L. Mai, *Adv. Energy Mater.* **2022,** *12*, 2103343. https://doi.org/10.1002/aenm.202103343.

[8] P. Zhang, Q. Zhu, Y. Wei, B. Xu, *Chem. Eng. J.* **2023,** *451*, 138891. https://doi.org/10.1016/j.cej.2022.138891.

[9] K. Yao, Z. Xu, M. Ma, J. Li, F. Lu, J. Huang, *Adv. Funct. Mater.* **2020,** *30*, 2001484. https://doi.org/10.1002/adfm.202001484.

[10] S. Chong, M. Ma, L. Yuan, S. Qiao, S. Dong, H. Liu, S. Dou, *Energy Environ. Mater.* **2022**, e12458. https://doi.org/10.1002/eem2.12458.

[11] X. Yin, Z. Lu, J. Wang, X. Feng, S. Roy, X. Liu, Y. Yang, Y. Zhao, J. Zhang, *Adv. Mater.* **2022,** *34*, 2109282. https://doi.org/10.1002/adma.202109282.

[12] X. Tao, J. Wang, C. Liu, H. Wang, H. Yao, G. Zheng, Z. W. Seh, Q. Cai, W. Li, G. Zhou, C. Zu, Y. Cui, *Nat. Commun.* **2016,** *7*, 11203. https://doi.org/10.1038/ncomms11203.

[13] J. Zhou, X. Liu, L. Zhu, J. Zhou, Y. Guan, L. Chen, S. Niu, J. Cai, D. Sun, Y. Zhu, J. Du, G. Wang, Y. Qian, *Joule* **2018,** *2*, 2681-2693. https://doi.org/10.1016/j.joule.2018.08.010.

[14] Q. Zhao, S. Stalin, L. A. Archer, *Joule* **2021,** *5*, 1119-1142. https://doi.org/10.1016/j.joule.2021.03.024.

[15] L. Fan, S. Chen, R. Ma, J. Wang, B. Lu, *Small* **2018,** *14*, 1801806. https://doi.org/10.1002/smll.201801806.

[16] Z. Bo, P. Chen, F. Tian, Y. Huang, Z. Zheng, J. Yan, K. Cen, H. Yang, K. Ostrikov, *Carbon* **2023,** *213*, 118261. https://doi.org/10.1016/j.carbon.2023.118261.

[17] L. Wang, J. Yang, J. Li, T. Chen, S. Chen, Z. Wu, J. Qiu, B. Wang, P. Gao, X. Niu, H. Li, *J. Power Sources* **2019,** *409*, 24-30. https://doi.org/10.1016/j.jpowsour.2018.10.092.

[18] D. Ba, Q. Gui, W. Liu, Z. Wang, Y. Li, J. Liu, *Nano Energy* **2022,** *94*, 106918. https://doi.org/10.1016/j.nanoen.2022.106918.

[19] B. Wang, H. Wu, L. Yu, R. Xu, T.-T. Lim, X. W. Lou, *Adv. Mater.* **2012,** *24*, 1111-1116. https://doi.org/10.1002/adma.201104599.

[20] M. Ma, L. Cao, K. Yao, J. Li, K. Kajiyoshi, J. Huang, *ACS Sustainable Chem. Eng.* **2021,** *9*, 5315-5321. https://doi.org/10.1021/acssuschemeng.0c09030.

[21] J. Pu, Y. Tan, T. Wang, W. Gong, C. Gu, P. Xue, Z. Wang, Y. Yao, *Small* **2023**, 2304847. https://doi.org/10.1002/smll.202304847.

[22] G. Yang, Y. Jiao, H. Yan, Y. Xie, A. Wu, X. Dong, D. Guo, C. Tian, H. Fu, *Adv. Mater.* **2020,** *32*, 2000455. https://doi.org/10.1002/adma.202000455.

[23] Y. Zhang, Z. Zhang, Y. Zhang, P. Wang, P. Han, K. Li, W. Liu, *Energy & Fuels* **2021,** *35*, 20330-20338. https://doi.org/10.1021/acs.energyfuels.1c02999.

[24] P. Zeng, F. Qian, Y. Lin, X. Wang, J. Li, W. Wang, F. Tao, Z. Fang, *Mater. Res. Express* **2018,** *5*, 025502. https://dx.doi.org/10.1088/2053-1591/aaa8c3.

[25] Z. Zheng, H.-H. Wu, H. Liu, Q. Zhang, X. He, S. Yu, V. Petrova, J. Feng, R. Kostecki, P. Liu, D.-L. Peng, M. Liu, M.-S. Wang, *ACS Nano* **2020,** *14*, 9545-9561. https://doi.org/10.1021/acsnano.9b08575.

[26] Z. Guo, X. Wang, *Angew. Chem. Int. Ed.* **2018**, *57*, 5898. https://doi.org/10.1002/anie.20180309.

[27] Z. Zhao, Z. Yi, Y. Duan, R. Pathak, X. Cheng, Y. Wang, J. W. Elam, X. Wang, *Chem. Eng. J.* **2023,** *463*, 142397. https://doi.org/10.1016/j.cej.2023.142397.

[28] K. Wu, L. Zhang, Y. Yuan, L. Zhong, Z. Chen, X. Chi, H. Lu, Z. Chen, R. Zou, T. Li, C. Jiang, Y. Chen, X. Peng, J. Lu, *Adv. Mater.* **2020,** *32*, 2002292. https://doi.org/10.1002/adma.202002292.

[29] L. Zhu, M. Wang, S. Xiang, D. Sun, Y. Tang, H. Wang, *Adv. Energy Mater.* **2023,** *13*, 2302046. https://doi.org/10.1002/aenm.202302046.

[30] J. Shen, X. Xu, J. Liu, Z. Wang, S. Zuo, Z. Liu, D. Zhang, J. Liu, M. Zhu, *Adv. Energy Mater.* **2021,** *11*, 2100673. https://doi.org/10.1002/aenm.202100673.

[31] B. Ma, P. Sittisomwong, J. Ma, P. Bai, *ACS Appl. Energy Mater.* **2022,** *5*, 7124-7133. https://doi.org/10.1021/acsaem.2c00716.

[32] C. Liu, Z. Yang, J. Sun, *Energy Storage Mater.* **2022,** *53*, 22-31. https://doi.org/10.2139/ssrn.4036513.

[33] L. Deng, Y. Zhang, R. Wang, M. Feng, X. Niu, L. Tan, Y. Zhu, *ACS Appl. Mater. Interf.* **2019,** *11*, 22449-22456. https://doi.org/10.1021/acsami.9b06156.

[34] X. Cheng, Y. Sun, D. Li, H. Yang, F. Chen, F. Huang, Y. Jiang, Y. Wu, X. An, Y. Yu, *Adv. Energy Mater.* **2021,** *11*, 2102263. https://doi.org/10.1002/aenm.202102263.

[35] X. Yi, A.M. Rao, J. Zhou, B. Lu, *Nano-Micro Lett.* **2023**, *15*, 200. https://doi.org/10.1007/s40820-023-01178-3.

[36] S. Liu, L. C. Meyer, L. Medenbach, A. Balducci, *Energy Storage Mater.* **2022**, *47*, 534-541. https://doi.org/10.1016/j.ensm.2022.02.041.

[37] J. Ge, C. Ma, Y. Wan, G. Tang, H. Dai, S. Sun, W. Chen, *Adv. Funct. Mater.* **2023**, *33*, 2305803. https://doi.org/10.1002/adfm.202305803.

[38] J. Ge, B. Wang, J. Wang, Q. Zhang, B. Lu, *Adv. Energy Mater.* **2020**, *10*, 1903277. https://doi.org/10.1002/aenm.201903277.

[39] Y. Yang, L. Wang, S. Zeng, K. Zhao, Q. Wu, L. Yan, H. Tian, Z. Jiao, J. Zhang, *J. Colloid Interf. Sci.* **2022,** *624*, 670-679. https://doi.org/10.1016/j.jcis.2022.05.129.

[40] Q. Tan, K. Han, W. Zhao, P. Li, Z. Liu, S. Li, X. Qu, *Sustain. Energ. Fuels* **2021,** *5*, 844-854. https://doi.org/10.1039/d0se01457e.

The table of contents entry:

Equilibrium "$E_a$-$E_b$" relationship, i.e., the moderate adsorption energy and lowest diffusion barrier originated from narrow Δ*p*-*d* band gap, as well as compatible electrolyte formula, is found to facilitate the most effective ionic transfer from the surface to the bulk of electrode with guaranteed capacity and redox kinetics.

Meng Ma, Kai Yao, Yikun Wang, Dina Fattakhova-Rohlfing, Shaokun Chong*

Decoupling the Kinetic Essence of Iron-Based Anodes through Anionic Modulation for Rational Potassium-Ion Battery Design

ToC figure